Radiation-hardness studies with cerium-doped fused-silica fibers

Published by IOP Publishing for Sissa Medialab

Received: *December 6, 2018*
Accepted: *March 9, 2019*
Published: *March 19, 2019*

Radiation-hardness studies with cerium-doped fused-silica fibers

N. Akchurin,[a] E. Kendir,[b] Ş. Yaltkaya,[b] J. Damgov,[a] F. De Guio[a] and S. Kunori[a]

[a] *Texas Tech University, Department of Physics and Astronomy, Lubbock, TX, 79409, U.S.A.*
[b] *Akdeniz University, Department of Physics, Antalya, 07070, Turkey*

E-mail: nural.akchurin@ttu.edu

Abstract: We describe our R&D effort to develop potentially radiation-hard scintillating and wavelength shifting fibers by doping fused-silica with cerium. The cerium-doped optical fibers with different core structures and concentrations were exposed to gamma radiation (^{60}Co) at different dose rates up to 100 kGy. We evaluated the radiation-induced degradation in photoluminescence, optical transmission, and recovery phenomena in the wavelength range from 300 to 700 nm. We were able to model the experimental data based on second-order rate equations where the fit parameters that govern the damage profile were utilized to predict recovery. We also measured the influence of radiation on the numerical aperture. Finally, we offer some thoughts on the use of these types of fibers in particle and nuclear physics detectors.

Keywords: Calorimeters; Radiation-hard detectors; Scintillators and scintillating fibres and light guides; Scintillators, scintillation and light emission processes (solid, gas and liquid scintillators)

[1]Corresponding author.

https://doi.org/10.1088/1748-0221/14/03/P03020

2019 JINST 14 P03020

Contents

2019 JINST 14 P03020

1 Introduction

Light emission by plastic scintillators typically degrades by half after a few MRads (a few 10 kGy). Our objective is to explore possible gains in radiation-hardness by doping fused-silica with inorganic "dyes" or rare-earth elements to produce scintillating and/or wavelength shifting fibers. Our experience [1–5] shows that clear (un-doped) fused-silica fibers survive large doses (O[10] MGy), and our preliminary results reported here, and those of others (for example, [6–15]), on doped fused-silica suggest that this approach is likely to result in meaningful progress because there has been accumulation of data complemented by improved understanding of radiation damage and light emission and absorption processes in these types of structures [16–18]. We described our results from the first two prototype fibers (so-called $S^{(1)}$ and $S^{(2)}$ fibers correspond to the Phase-I and -II fibers in this paper) in an earlier publication [19]. In this paper, we report on the performance of additional fibers, Phase-III, Phase-IV, and T14, and especially on their behavior under gamma irradiation. Clear fused-silica fiber containing no dopants was also included as benchmark. This fiber is the same fiber as in the active medium of CMS's forward calorimeter, and its radiation-hardness properties were well-studied and reported in scientific literature. All fibers reported here are produced by Polymicro Technologies.[1]

2 Description of fibers

The first large-scale (> 1 km) cerium-doped fiber production in this study was that of Phase-I fiber. The cerium-doped core was 60 μm in diameter and enveloped by a 200 μm diameter coaxial glass layer. The core preform was doped with cerium by a proprietary dissolving method, and the

[1]Polymicro Technologies is a subsidiary of Molex located in Phoenix, AZ, U.S.A..

Ce:Si molar ratio was $\sim 10^{-3}$. Phase-II fiber was essentially the same as Phase-I except for a larger central core (150 μm dia.). This fiber was also produced at a large scale (~2 km) using standard industrial techniques.

The core of the Phase-III fiber was Ce-doped (370 μm dia.) but without a glass layer around it. This fiber was produced to evaluate the efficacy of the clear glass layers in Phase-I and -II fibers in terms of light transport. Phase-IV fiber was produced with a 15-μm thick Ce-doped ring around a 200-μm diameter clear fused-silica core. In addition, a 600-μm diameter glass outer layer was introduced to further improve light transmission. The T14 fiber's Ce-doped core (150 μm dia.) was surrounded by a high OH^- fused-silica layer (400 μm dia). In contrast, the outer layers in Phase-I and -II fibers were composed of low OH^- glass.

Table 1 summarizes the dimensions of core, glass, cladding, and buffer while figure 1 shows the fiber cross-sectional images. Some performance characteristics of Phase-I and -II fibers that were measured with the high energy beams at Fermilab were reported in our first paper [19]: for example, the Phase-I optical attenuation length measured about 5.8 ± 0.7 m using 16 GeV electrons. The speed of light propagation was 19.50 ± 0.38 cm/ns and was found to be consistent with the previously reported values [20, 21]. When the tail of the pulse was modeled by a sum of two exponential functions, two decay constants were $\tau_1 = 20.8 \pm 5.4$, and $\tau_2 = 93.0 \pm 12.6$ ns. The contributions of these components to the total light emission (radioluminescence) turned out to be $23.9 \pm 5.3\%$ and $76.1 \pm 5.3\%$, respectively.

Table 1. All fibers were cladded with fluorinated acrylate and UV-cured acrylate buffer.

Fiber Name	Core OD [μm]	Glass OD [μm]	Clad OD [μm]	Buffer OD [μm]
Phase-I	60±7	200±6	230^{+5}_{-10}	350±15
Phase-II	150±20	400±10	430±10	550±30
Phase-III	370±8	—	400 ±8	550±15
Phase-IV	200±8(clear) 230±8(doped)	600±6	630±10	800±30
Clear fused-silica	600±10	—	630^{+5}_{-10}	800±30
T14	150±5	400±5	450±5	500±15

Laser ablation inductively-coupled plasma mass spectrometry (Agilent 7500cs) was used to determine the chemical composition of all fibers (table 2). The fibers were scanned across at the rate of 5 μm/s with a laser 40-μm diameter spot size. The laser delivered ~7.5 J/cm^2 per pulse. The cerium concentration was measured in Phase-I, -II, -III and T14 cores, and the Phase-IV ring structure (figure 2). Along with Ce in the doped-core, we observed small concentrations of Ga, La, and Gd, which tend to accompany Ce in glasses. Significant concentrations of Al in Phase-I, -II, and T14 cores were also evident.

3 Irradiation setups

The irradiation studies were performed in two different ways. In the first case, single 2.5 m long Ce-doped and clear fused-silica fibers were each spooled into a 15-cm diameter circle and exposed

2019 JINST 14 P03020

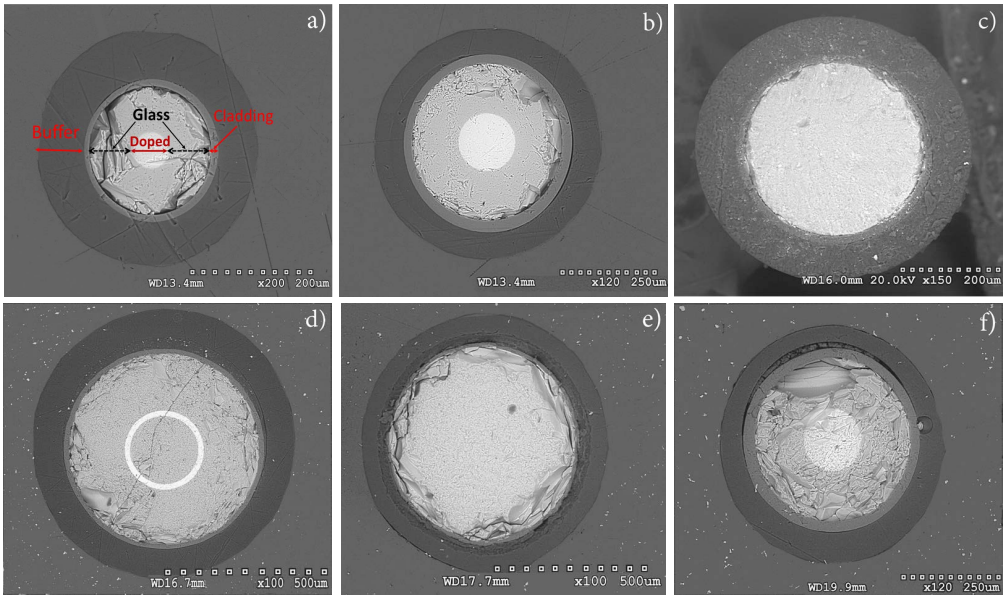

Figure 1. The cross-section of fibers (a) Phase-I, (b) -II, (c) -III, (d) -IV, (e) clear fused-silica, and (f) T14 are shown. The terminology used throughout the paper for different parts of the fiber is indicated on (a).

to total doses of 0.5, 5, 10, or 100 kGy at rates of 0.05, 0.5, 1, or 10 kGy/h, respectively, at the University of Maryland Gamma Irradiation Facility. After irradiation, the spectra were obtained from all fibers and compared to their individual spectra recorded before irradiation. We used the pulsed xenon light source (PX-2) and a spectrometer (USB2000), both from Ocean Optics, for these measurements. In all measurements, the dark count was subtracted and the spectrometer was properly calibrated to take quantum efficiencies as a function of wavelength into account.[2] The spooled fibers were stored in clear plastic bags at ambient temperature.

In the second case, where the accumulated doses were considerably lower compared to the first case, we measured the radiation-induced losses online, i.e. as the fibers were being exposed to gamma radiation. The clear fused-silica transfer fibers of 6-m length were connected to both ends of the fiber spool being tested. One end was connected to a light source (a 6.5-W tungsten-halogen lamp with an optical chopper), and the other was connected to the spectrometer (USB2000). The spectrometer and optical chopper were controlled by a common trigger in order to synchronize the data taking with the light injection. The spectrometer, light source, and optical chopper were placed in a thick lead enclosure and well-protected from radiation. The dose rate was determined by the proximity of the fiber spool to the radioactive source, and measurements were made at the rates of 5, 25, 106, 402, and 1,007 Gy/h. In this configuration, the total doses up to 400 Gy were recorded. Figures 3(a) and (b) show the tungsten-halogen and xenon spectra transmitted through 2.5 m of un-irradiated fibers, respectively.

4 Photoluminescence and attenuation measurements

Figure 4 shows the photoluminescence response of the fibers to axially injected 337 nm laser pulses from a pulsed N_2 laser soon after they were irradiated. The N_2 laser emission is near the known

[2] https://oceanoptics.com/wp-content/uploads/USB2000-Operating-Instructions.pdf

2019 JINST 14 P03020

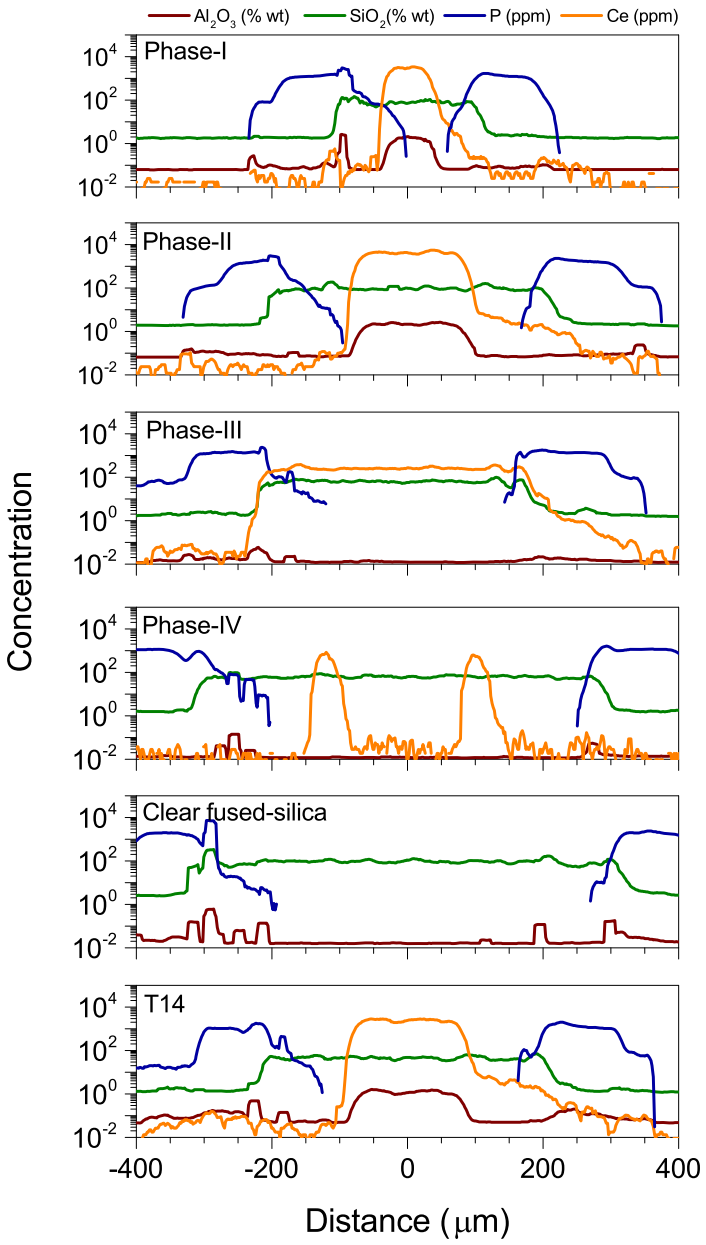

Figure 2. The Si, Al, P, and Ce concentrations in different parts of the Phase-I, -II, -III, -IV, clear fused-silica, and T14 fibers are clearly visible as the laser ablates material and rasters across the fibers. The presence and location of Ce is indicated by the solid orange lines. The presence of Al is also evident in Phase-I, -II, and T14 fibers. Al in Phase-III, -IV, and clear fused-silica fibers is not significant. The P concentration is dominant in all acrylate cladding and buffer and also appears in the core of the Phase-I and -II fibers. As can be deduced from the signal asymmetry, the laser scan direction is from left to right, and the right-side tail indicated the continued flow of ablated material into the spectrometer as the laser spot moves at constant speed across the fibers. The vertical axis indicates percentage molar weights for Al and Si but ppm for P and Ce for some example scans.

2019 JINST 14 P03020

Table 2. The chemical concentrations from different regions of the fibers are measured using a laser ablation inductively-coupled plasma quadrupole mass spectrometer. The values are in ppm. No quantitative data are listed if the measurement is below the spectrometer detection level.

Fiber	Mg	Al_2O_3	P	Sc	Ti	Ga	La	Ce	Gd
Phase-I doped	433	19,200	120	2	10	42	1	3,394	2
Phase-I glass	65	39	326	1	—	—	—	—	—
Phase-I clad	14	296	2,197	—	—	—	—	—	—
Phase-I buffer	13	486	163	—	—	—	—	—	—
Phase—II doped	—	26,141	22	2	—	57	1	4,830	2
Phase-II glass	80	81	60	2	1	—	1	1	—
Phase-II clad	30	195	2,686	—	1	—	—	—	—
Phase-II buffer	6	567	211	—	—	—	—	—	—
Phase—III doped	3	31	—	2	—	4	—	237	—
Phase-III clad	4	253	1,768	—	—	—	—	—	—
Phase-III buffer	4	75	81	—	—	—	—	—	—
Phase-IV core	2	27	—	2	—	—	—	—	—
Phase-IV ring	30	393	—	2	4	9	—	793	—
Phase-IV glass	7	14	—	2	—	—	—	—	—
Phase-IV clad	3	90	1,444	—	—	—	—	—	—
Phase-IV buffer	9	58	38	—	1	—	—	—	—
Clear fused-silica core	6	56	22	3	—	—	—	—	—
Clear fused-silica clad	31	1,117	2,563	—	1	—	—	—	—
Clear fused-silica buffer	31	953	71	—	6	—	—	—	—
T14 doped	16	13,888	—	1	—	34	1	2,961	1
T14 glass	10	86	—	2	—	—	—	—	—
T14 clad	18	1,124	1,862	—	1	—	—	—	—
T14 buffer	14	264	77	—	—	—	—	—	—

~320 nm absorption band of cerium. Several salient features were revealed by this measurement. Prior to irradiation, the cerium-doped fibers clearly showed broad emission peaks at around 420 and 460 nm (solid black lines). The Phase-III and -IV fibers' emission spectra differed from those of others (Phase-I, -II, and T14) by having shifted to longer wavelengths by about 20 nm (red-shifted). We ascribe this difference to the absence of Al in these two fibers [22, 23]. In all cases, the double-peak structure was apparent perhaps indicating locally ordered crystalline structure in the immediate vicinity of cerium as opposed to a more common single broader peak in the case of disordered glasses. The XRD measurements ruled out the possibility of local ordered structures. The two known Ce^{3+} emission lines are due to transitions from the lowest 5d to the 4f levels where the spin-orbit coupling splits the transition into two (^2F_J = 7/2 and 5/2). These states differ by ~2,200 cm^{-1} and the observed double-peak structure is consistent with this difference in all cases. We have also tested these fibers by exciting under UV (Philips UV 30/G30 TB) and

2019 JINST 14 P03020

X-ray (Tungsten 32 kV) which result in generally consistent line shapes but with slight differences that are currently under investigation. The transmission of unabsorbed laser light, centered around 337 nm, through the glass parts of the fibers was also apparent. No optimization in the selection of the glass part was carried out in terms of radiation-hardness for Phase-I and -II fibers. The T14 fiber, on the other hand, was made using relatively high OH^- fused-silica (~400 ppm) for its glass part. Although the generation and transmission of wavelength shifted light suffered, there was good indication that the fiber had not been completely damaged. The Phase-IV fiber, on the other hand, performed significantly better. There was a gradual loss of performance with increasing dose; however, the transmission of UV light and emission (and transmission) of the wavelength shifted light were clearly visible even after 100 kGy. Naturally, the fiber structure was optimized for light transmission with a coaxial clear core (~700 ppm OH^-) and a glass layer (~400 ppm OH^-) around the thin Ce-doped ring (130–220 ppm OH^-). As can be gleaned from these data, the degree of transmission of the UV light can be discerned from the (saturated) peak around 337 nm and the degree of photoluminescence from the emission curves at >400 nm. The clear fused-silica fiber (~700 ppm OH^-) was included as comparison in this analysis: as expected, there is no indication of photoluminescence, and the UV light is transmitted with good efficiency. The level of attenuation at 100 kGy is consistent with previously published data (~0.05 dB/m at 430 nm) [1].

The radiation-induced attenuation at a given wavelength λ and accumulated dose D is calculated in the customary fashion:

$$A(\lambda, D) = -\frac{10}{L} \log\left(\frac{I(\lambda, D)}{I_o(\lambda)}\right) \tag{4.1}$$

where A is attenuation [dB/m], L is the exposed fiber length [m], I is the transmitted light intensity at the integrated dose D, and I_o is the transmitted light intensity for an un-irradiated ($D = 0$) fiber. The transmission, T, equals $\frac{I(\lambda,D)}{I_o(\lambda)}$.

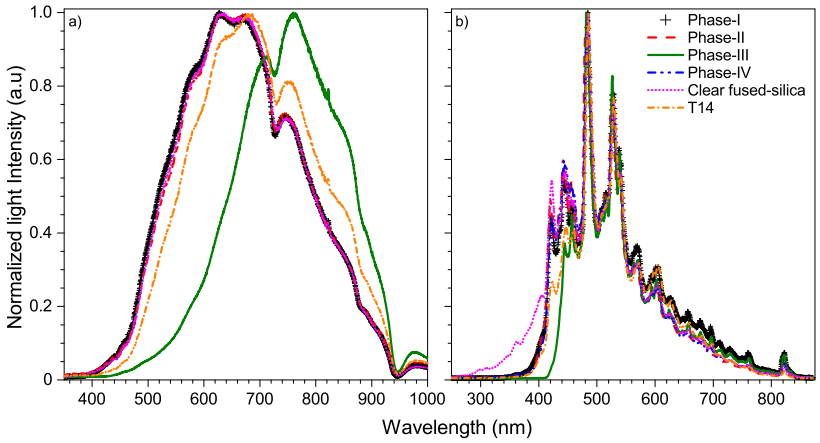

Figure 3. The measured spectra using (a) tungsten-halogen and (b) xenon light sources display interesting features. The clear fused-silica fiber spectra are shown in dotted red lines. The transparency to shorter wavelengths ($\lambda \leq 400$ nm) is especially apparent in the case of the xenon lamp. The fibers that have glass layers around the cerium-doped core (Phase-I and -II), or additionally contain a clear central core (Phase-IV) also effectively transmit light without strong wavelength shifting. In contrast, Phase-III fiber, which does not contain any clear fused-silica component, shows clear evidence of absorption of short wavelengths. All spectra are normalized to unity at their maxima.

2019 JINST 14 P03020

Figure 4(g) to (k) panels display the levels of photoluminescence and optical attenuation of irradiated fibers at four wavelengths (430, 470, 500, and 600 nm) when excited by 337-nm photons. For example, Phase-I fiber attenuation increased very rapidly and reached saturation at 9 dB/m. The saturation plateau dropped from 9 to 7.5 dB/m for the longer wavelengths. Similar behavior was observed for Phase-II and T14 fibers. Phase IV was distinctly different, ~4 dB/m at 100 kGy, whereas the clear fused-silica attenuation was drastically better, ~0.2 dB/m at the same accumulated dose.

The presence of aluminum and phosphorus in the Ce-doped core seems significant in terms of radiation-hardness. For example, Phase-IV fiber contained essentially no aluminum and phosphorus and was significantly better in terms of preserving its photoluminescence and light transport performance compared to Phase-I, -II, and T14. Fox and collaborators found that otherwise radiation-hard Yb-doped fiber lost its radiation resistance when Al, Ge, and P were introduced into the fiber core [24]. Faustov et al. reported that Al and P doped fibers showed high sensitivity to radiation compared to the rare-earth doped only fibers [25]. Similarly, others also reported degradation in radiation resistance in the presence of metals such as Ti, Co, and Fe [26–28]. The likely mechanism is as follows: if Al^{3+} replace the Si^{4+} ion as substitutional, it will require charge compensation. In fused-silica, several types of compensators, such as H^+, Li^+, or Na^+ ions, are present at interstitial sites or holes trapped at oxygen ions. Due to strong attractive interaction between the interstitial ions and the holes with the aluminum ion, and to the mobility of both interstitial ions and holes, these charge compensators reside near the substitutional aluminum ion and form color centers with a broad absorption spectrum [23, 29].

The optical transmissions by these fibers are displayed in figure 5. For the same wavelengths and accumulated doses, the level of attenuation was considerably smaller in this case compared to figure 4(g)–(k) because there was no strong photoluminescence. The same four wavelengths were selected from the broad spectrum of xenon light for this measurement. As expected, the clear fused-silica fiber performed in the same way as there was no dopant to introduce photoluminescent light into the fiber. It is also worth noting that the difference in "attenuation" is the largest for Phase-I and -II fibers, and the least for Phase-IV fiber when figures 4 and 5 are compared.

4.1 Modeling of radiation-induced damage and optical recovery

The radiation-induced attenuation expressed in equation 4.1 can be recast as:

$$A(\lambda, D) = -\frac{10}{L}\log T = a\left(\frac{D}{D_{\mathrm{r}}}\right)^{b} \tag{4.2}$$

where a is in units of dB/m, b is a constant $(0 < b < 1)$, and D_{r} can be taken as a reference dose at which $A = a$. When the transmission is expressed alone, we have

$$T = \exp\left[-\frac{aL}{4.34}\left(\frac{D}{D_{\mathrm{r}}}\right)^{b}\right], \tag{4.3}$$

a "stretched exponential" Kohlrausch function. Several approaches for modeling the radiation-induced optical attenuation and recovery processes of doped and un-doped optical fibers have been reported in recent decades [30–33]. Our aim is to adhere to one coherent formulation for the growth of radiation-induced attenuation and the recovery of optical transmission after irradiation

2019 JINST 14 P03020

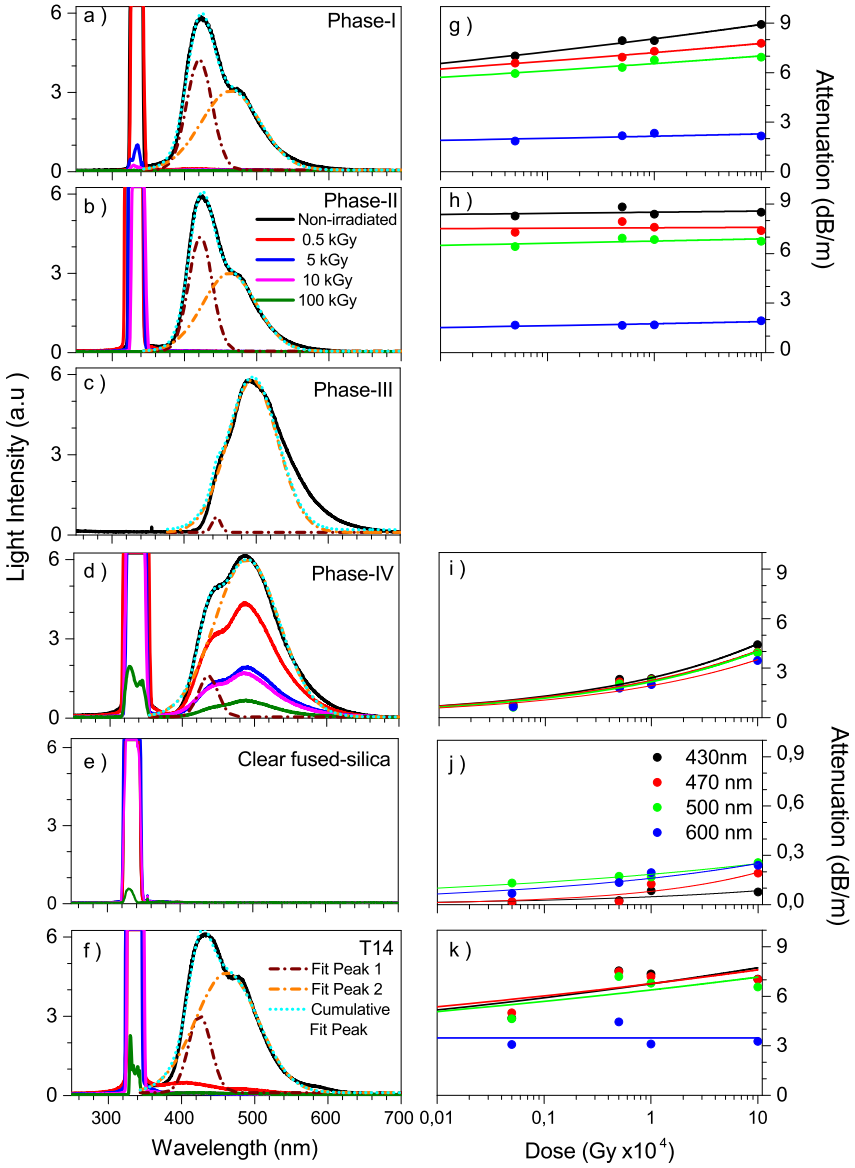

Figure 4. Gamma-irradiated Phase-I, -II, -IV, clear fused-silica, and T14 fibers show varied levels of loss of transmission and photoluminescence when the fibers are excited at 337 nm as displayed in panels (a) to (f) on the left column (N_2 laser light axially injected into the fibers). Phase-III fiber (un-irradiated) spectrum is included for comparison and it is worth noting that there is no transmission of the laser light at 337 nm, as this fiber does not have a clear glass component. Dash-dotted lines indicate gaussian fits, two individual components, with mean values at near 420 (brown) and 460 (orange) nm. The dotted blue line is the sum of the two, and in good agreement with the measured spectra (solid black line). On the right column, panels (g) to (k), the attenuation measurements are given at four different wavelengths. Note the difference in vertical scale (1/10) in panel (j) displaying a small radiation-induced optical transmission loss for the clear fused-silica fiber compared to the doped fibers. These measurements were carried out five days after the irradiation campaign.

2019 JINST 14 P03020

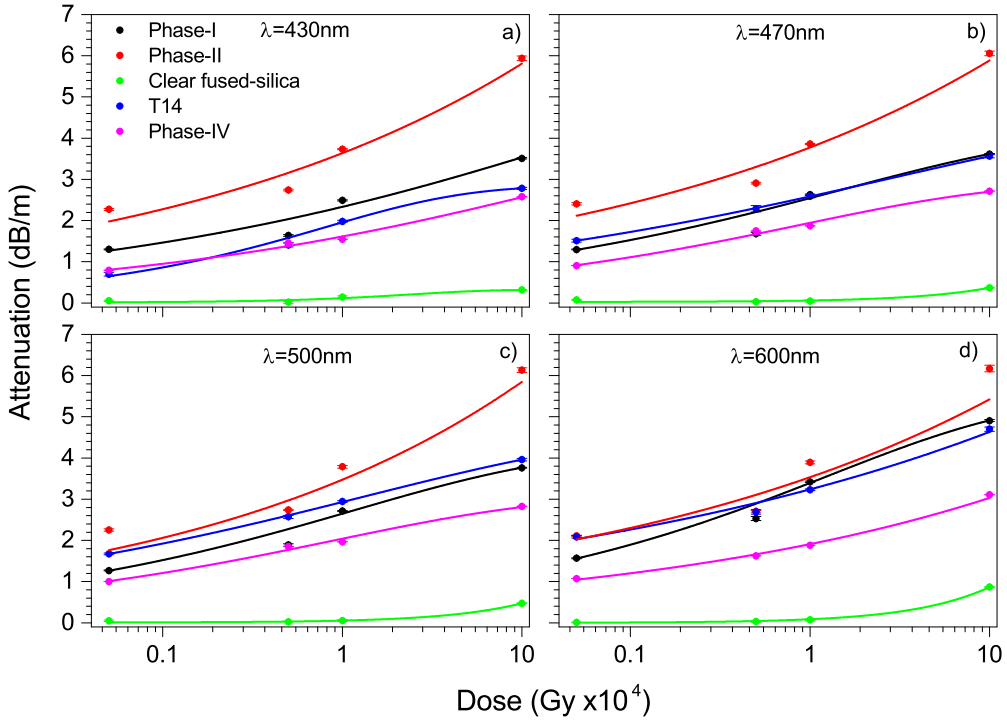

Figure 5. The optical transmission measurements at four different wavelengths were made by axially injecting pulsed xenon light and measuring the spectra at the end of the fibers. These measurements were carried out five days after the irradiation campaign. The solid lines are drawn to guide the eye.

has ceased. We follow Griscom's classical rate equation for second-order growth with thermally activated decay approach [34]:

$$dN(t)/dt = K\dot{D}N^* - RN^2/N^* \tag{4.4}$$

with its solution

$$N(t) = N_{\text{sat}} \tanh(kt) \tag{4.5}$$

where $N_{\text{sat}} = (K\dot{D}/R)^{1/2}N^*$ and $k = (K\dot{D}R)^{1/2}$. N stands for the number density of color centers, $R = 1/\tau$ is the decay rate constant, K governs the creation of new color centers, N^* has the dimensionality of the color center number density. The "stretched" version of the second-order growth kinetics is accomplished by the $kt \rightarrow (kt)^\beta$ substitution where kt is dimensionless.

$$dN[(kt)^\beta]/d(kt)^\beta = (K\dot{D}/R)^{\beta/2}N^* - (R/K\dot{D})^{\beta/2}N^2/N^* \tag{4.6}$$

with $0 < \beta < 1$ and $k = (K\dot{D}R)^{1/2}$. The solution is

$$N[(kt)^\beta] = N_{\text{sat}} \tanh[(kt)^\beta]. \tag{4.7}$$

Here, $N_{\text{sat}} = (K\dot{D}/R)N^*$ and $k = (K\dot{D}R)^{1/2}$. The classical time-independent rate constant K and β are determined by fitting the experimental data. The recovery in this system of equations is

$$dN[(Rt)^\beta]/d(Rt)^\beta = -N^2/N^* \tag{4.8}$$

2019 JINST 14 P03020

with solution

$$N[(Rt)^{\beta}] = N(0)\{1 + [N(0)/N^{*}](Rt)^{\beta}\}^{-1}. \tag{4.9}$$

The analysis strategy is such that the radiation-induced attenuation data are first fitted using equation 4.7 to estimate N_{sat}, k, and β parameters. Based on these parameters, the optical recovery is predicted using equation 4.9. In what follows, we discuss the radiation-induced attenuation data from the Phase-I, II, III, clear fused-silica and T14 fibers in the context of this approach.

Figures 6 to 11 display data collected in online configuration as explained in section 3, i.e. the radiation-induced losses were measured as the fibers were being exposed to gamma irradiation. The optical attenuation and recovery data along with the fit and prediction curves (solid red lines) for the Phase-I fiber are shown in figure 6. The agreement between the data and formulation is good, capturing all salient features of both damage and recovery.

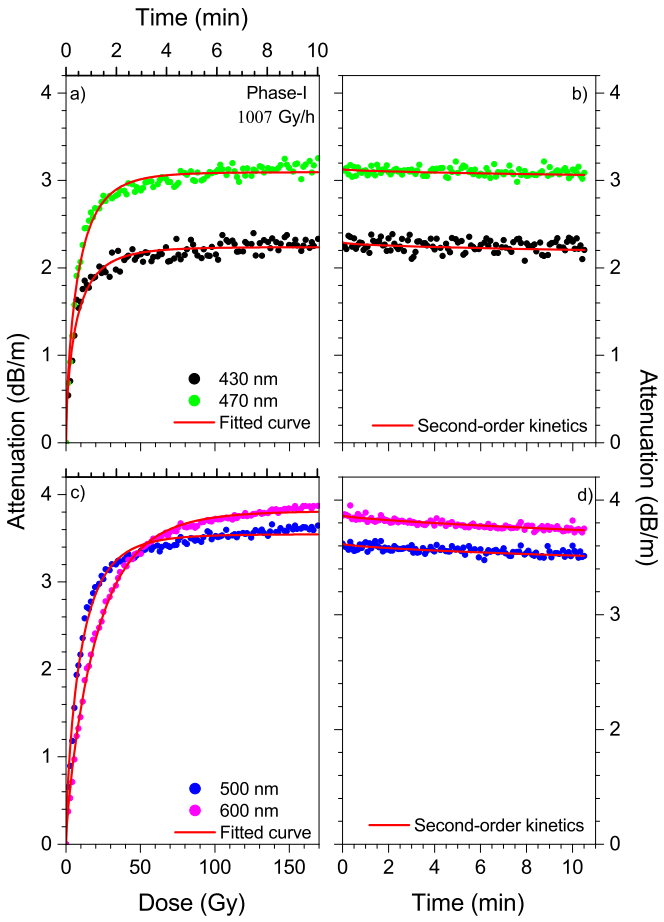

Figure 6. The radiation-induced attenuation (a) and (c), and recovery (b) and (d) for the Phase-I fiber at the 1007 Gy/h displays characteristic behavior of rapid increase with the accumulated dose at all wavelengths. The red curves in (a) and (c) are fits whereas in (b) and (d) are predictions, based on equations 4.7 and 4.9, respectively.

Figure 7 shows the radiation-induced attenuation and recovery for the Phase-II fiber. The attenuation is about 2 dB/m at short wavelengths and 0.7 dB/m at long wavelengths. The chemical compositions of Phase-I and Phase-II fibers are essentially the same except for the diameters of the

core, cladding, and buffer. Figures 7(b) and (d) show the optical recovery within 5 minutes after irradiation. The model for the damage and recovery processes describe the experimental data well, despite the fact that a couple of data points in the beginning appear poor, as accentuated by the solid red curves.

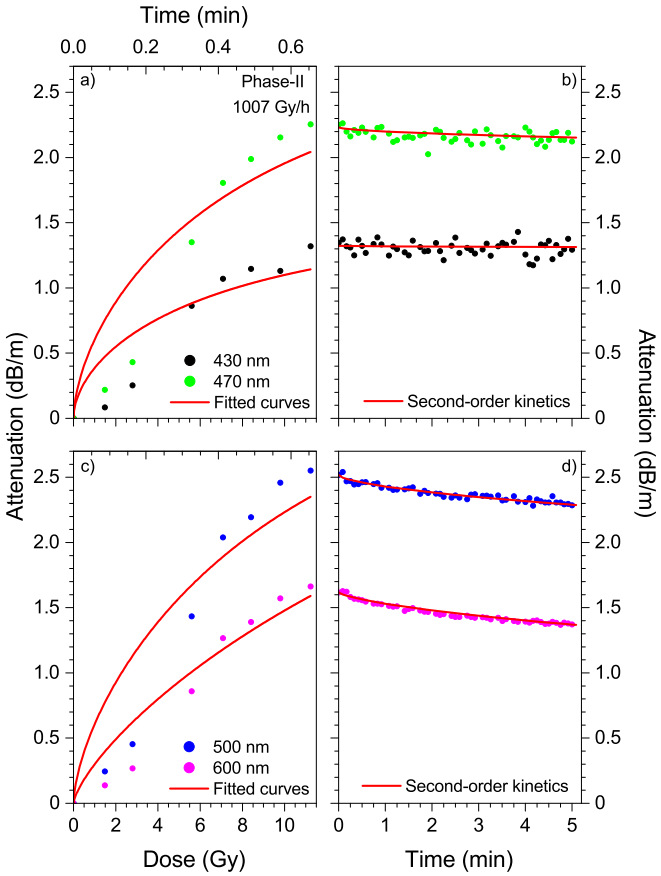

Figure 7. The panels (a) and (c) display the radiation-induced attenuation data for the Phase-II fiber under gamma irradiation at the rate of 1,007 Gy/h, and the panels (b) and (d) show recovery. The red solid lines are fits (equation 4.7) in panels (a) and (c), and predicitions (equation 4.9) in panels (b) and (d).

In addition to aluminum, the presence of phosphorus in both the doped core and glass layers prevented a rapid recovery process in Phase-I and -II fibers [35, 36]. The formation of color centers P_1 (oxygen vacancy centers) and POHC (phosphorus oxygen hole centers) seem responsible for this [37]. The defects due to POHC transform the phosphorus-related defect centers at a low dose rate [38]. The charges released by the POHC defects are re-trapped by the P_1 centers. Here, phosphorus' valence state (5+) is higher than that of silicon's (4+), and it provides a trapping potential for an electron. This state causes more oxygen bridging than silicon, thereby making POHC and P_1 related defects stable [38].

Figure 8 displays the Phase-III fiber radiation-induced attenuation and recovery measurement for 10 hours after irradiation. As in the case of the Phase-I and -II fibers, the radiation-induced attenuation (solid red line) data are well represented by equation 4.7. The recovery predictions, however, failed to represent the data adequately after an hour of recovery. The absence of phosphorus

2019 JINST 14 P03020

compared to the Phase-I and -II fibers was likely responsible for this behavior, where the recovery actually exceeded the initial level of attenuation.

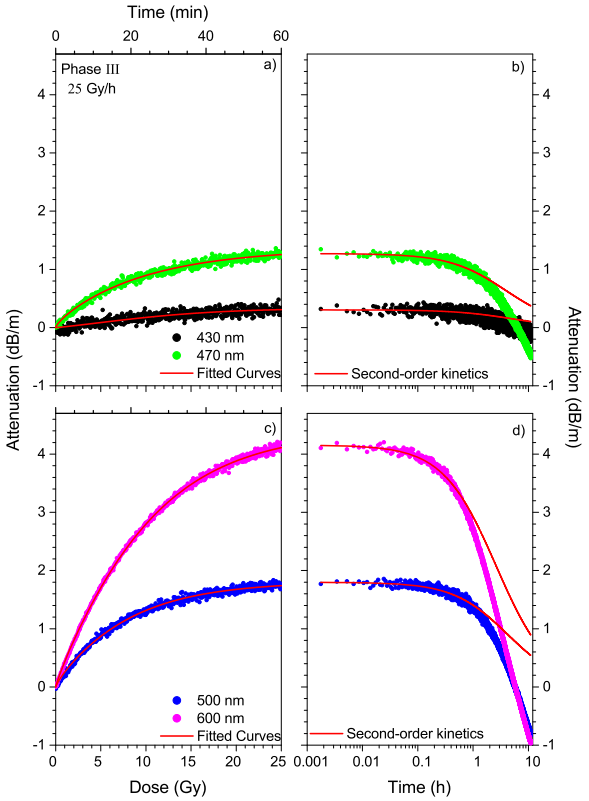

Figure 8. The radiation-induced attenuation (a) and (c) and 10-hour recovery (b) and (d) of the Phase-III fiber after the irradiation at a dose rate of 25 Gy/h. The solid red lines are fitted and predicted curves as indicated earlier.

Figure 9 shows the radiation-induced attenuation for the clear fused-silica fiber. A total dose of 250 Gy was applied to these fibers, and as in the previous cases, the radiation-induced attenuation data are fitted using equation 4.7. The radiation-induced attenuation of the clear fused-silica fiber is about one percent that of Ce-doped fibers. The 73-minute period after irradiation resulted in up to 50% recovery: rapid in the first ~ 10 minutes, followed by a slower recovery (figures 9.*b* and *d*).

4.2 Dose-rate dependence

The dose-rate dependence of radiation-induced degradation in different types of optical fibers have been investigated by several workers [26, 39–41]. At relatively low dose-rates, we were able study this phenomenon using the Phase-III and T14 fibers online. Figures 10 and 11 show the levels of radiation-induced attenuation as a function of different dose rates (5 to 1,007 Gy/h) at four selected wavelengths and accumulated doses. At all wavelengths, the attenuation increases as a function of dose and reaches a plateau. The degree of attenuation at this plateau depends on the wavelength. For example, at large dose rates (106, 402, and 1,007 Gy/h), the attenuation rises quickly and thereafter remains constant. The general attenuation behavior is similar at longer wavelengths. The data also

2019 JINST 14 P03020

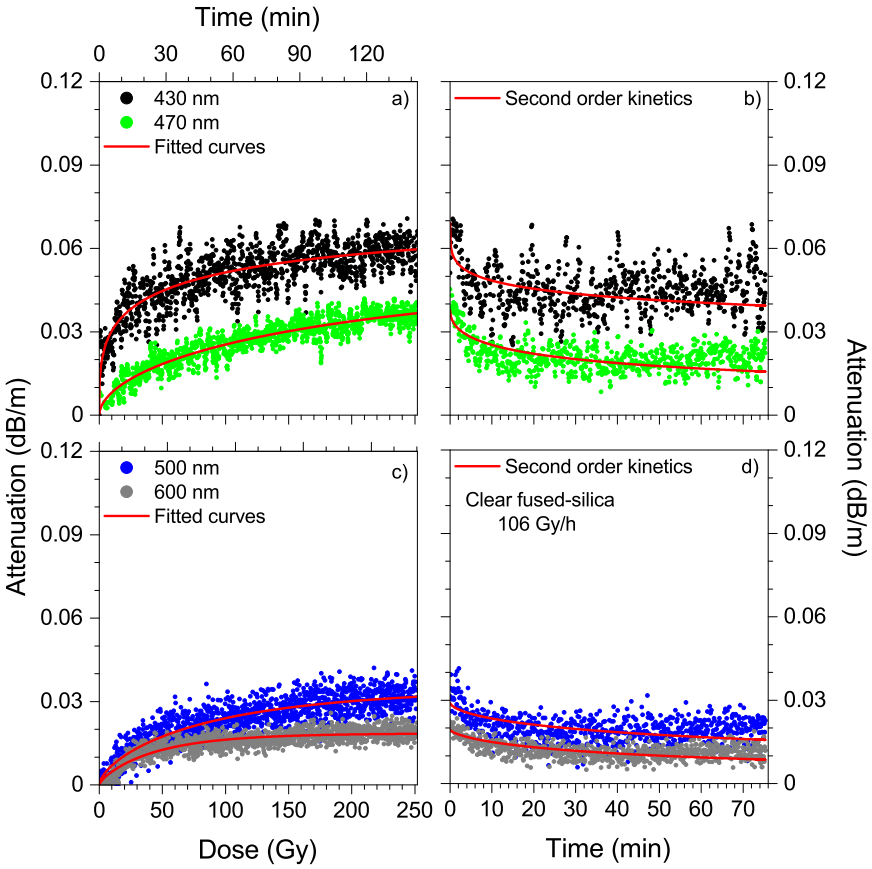

Figure 9. The radiation-induced attenuation of clear fused-silica fiber under gamma irradiation at 106 Gy/h dose rate is shown in panels (a) and (c). The panels (b) and (d) display the recovery in 73 minutes after irradiation. The black, green, blue and gray dots indicate wavelengths of 430, 470, 500 and 600 nm, respectively.

show that radiation sensitivity is less for shorter wavelengths. In addition to the radiation-induced attenuation measurements up to 400 Gy, figure 11 summarizes the optical recovery for about three hours after irradiation.

Figures 12 summarizes the parameters obtained after a fitting procedure to the radiation-induced attenuation data displayed in figures 10 and 11 for Phase-III and T14 fibers. The β parameter is the dimensionless exponent of (kt) that appears in the second-order differential equations and their solution. The k parameter, effective rate constant, scales linearly with the dose rate. In both cases (Phase-III and T14), β tends to decrease with the increasing dose rate, from near unity at the lowest dose rates to roughly 0.5 (T14) to 0.85 (Phase-III) at the high end. The N_{sat} parameter is a measure of color center density, or radiation-induced attenuation, at infinite time ($t \rightarrow \infty$).

5 Changes in effective numerical aperture

In order to determine the radiation-induced changes in the numerical aperture of the fibers, we used a simple setup. These measurements are straight-forward and potentially provide useful and complementary information in the use of Ce-doped fused-silica fibers in different applications. The

2019 JINST 14 P03020

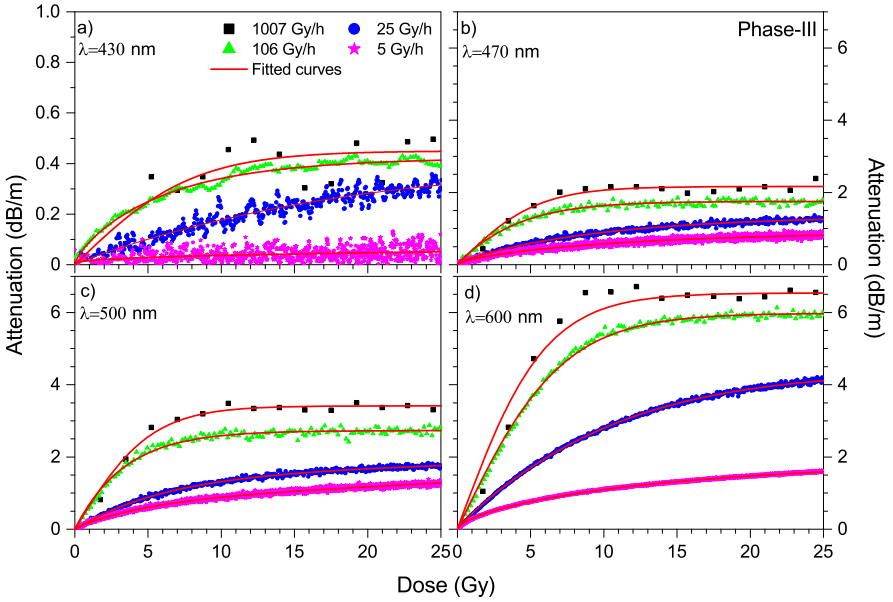

Figure 10. The optical attenuation at four different wavelengths under gamma ray irradiation at four different dose rates are shown for Phase-III: (a) 430 nm, (b) 470 nm, (c) 500 nm, and (d) 600 nm. The black, green, blue, and red symbols indicate dose rates of 1,007, 106, 25, and 5 Gy/h. The solid red lines are fits to the data as discussed in section 4.1.

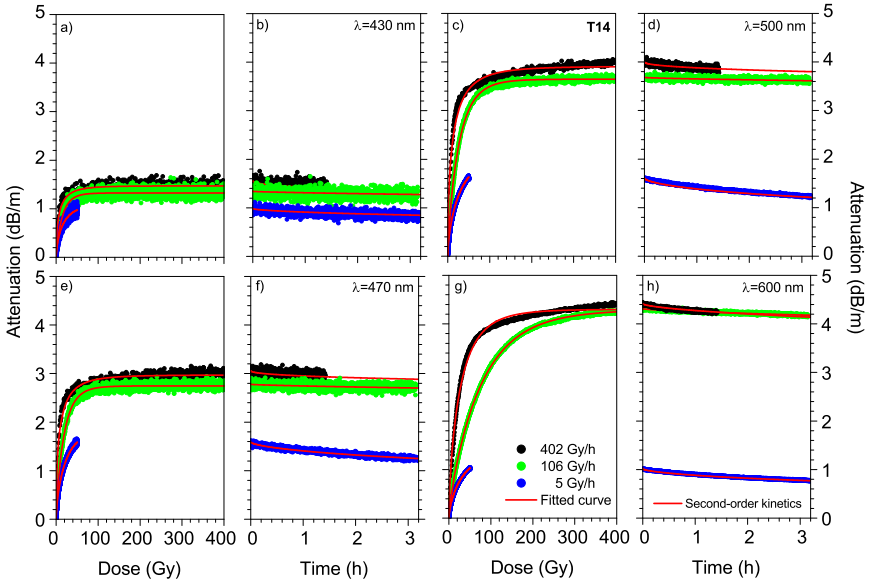

Figure 11. The radiation-induced attenuation of T14 fiber at 430, 470, 500, and 600 nm are shown in panels (a), (c), (e), and (g). The recovery of transparency within a 3-hour period at the same wavelengths are given in panels (b), (d), (f), and (h). The black, green, and blue dots indicate the dose-rates of 402, 106, and 5 Gy/h, respectively. The solid red lines are fits to the data on panels (a), (c), (e), and (f), but represent recovery prediction in panels (b), (d), (f), and (h), as discussed in section 4.1.

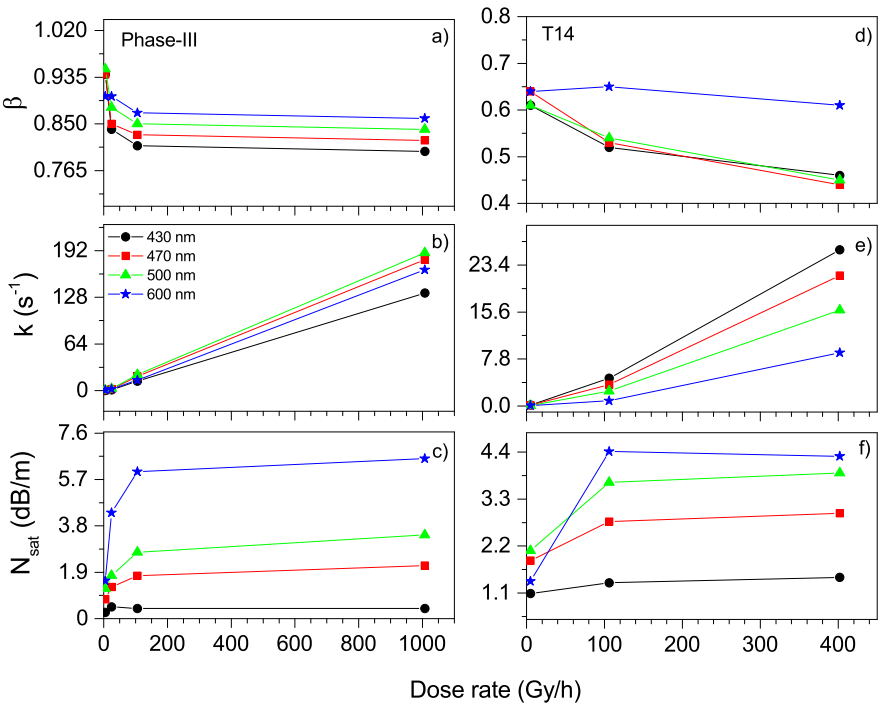

Figure 12. The behavior of fit parameters, β, k, and $N_{\rm sat}$ for the Phase-III on the left and T14 fibers are given as a function of dose rate on the right column. See section 4.1 for details.

fiber was positioned on a rotation stage, fiber tip at the central pivot point, driven by a stepping motor. The HeNe laser (Thorlabs HNL100L) beam was directed at the fiber tip. The light intensity was measured as a function of angle by a optical powermeter at the far end of the fiber.

The numerical aperture (NA) is expressed as $NA = \sin\theta_{\rm max} = \sqrt{n_{\rm co}^2 - n_{\rm cl}^2}$ where $n_{\rm co}$ and $n_{\rm cl}$ are the refractive indices of the core and cladding, respectively. The maximum incident angle, at which the light ray undergoes total internal reflection within the fiber, is $\theta_{\rm max}$. The difference in numerical apertures between the un-irradiated and irradiated fibers can be seen in figure 13. In order to calculate the numerical aperture, we first normalized the peak positions to unity, evaluated NA at $1/2e^2 \approx 0.068$ on either side of the peaks, and averaged the two. This prescription somewhat avoided small background noise at the tails and reduced the systematic error in fiber alignment on the rotation stage. Although the uncertainties are somewhat large and conservative, the central values indicate up to a 20% increase in numerical aperture with irradiation for the Ce-doped fibers, suggesting that $-dn_{\rm co}/dD > -dn_{\rm cl}/dD$. The reduction in the numerical aperture of the clear fused-silica fiber is small or negligible within the precision of the measurement but notable in that it is in the opposite direction of the doped fibers'.

6 Conclusions

Based on what we learned from a limited number of sample fibers, we are able to make the following statements thus far:

- The coaxial outer glass layer and central core (e.g. Phase-IV) improve light transmission and effective radiation-hardness. Although the light emission, i.e. photo- or radio-luminescence,

2019 JINST 14 P03020

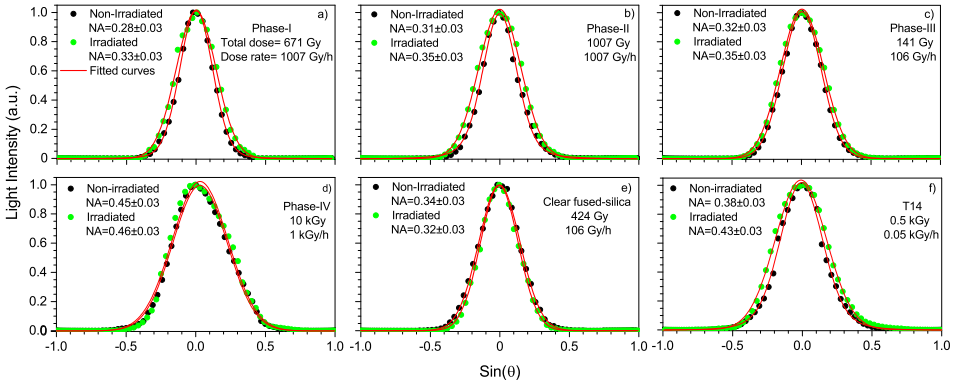

Figure 13. The radiation-induced changes in NA for six fibers (see table 1) are displayed before (back circles) and after (green circles) irradiation. The dose rates and accumulated doses are indicated on each plot. The solid red lines are gaussian distribution fits to the data points.

might suffer locally due to radiation, these structures help transport light through the radiation-hard (high OH^-) glass parts, circumventing self-absoption.

- The purity of materials is essential for improved radiation-hardness. The presence of aluminum and phosphorus tend to render fibers radiation-soft. Compared to the industry-standard radiation-hard clear fused-silica fiber, the best of cerium-doped fibers (Phase-IV) still need to be improved to be truly considered radiation-hard. For some applications, Phase-IV may be adequate if the accumulated dose is moderate (<100 kGy,).

- In the considered regimes in this paper (accumulated doses, dose rates, recovery times, wavelength ranges, etc.), a system of second-order kinetics rate equations appears to model the radiation-induced attenuation and recovery behavior well. For typical detector applications in particle and nuclear physics, we are concerned with the long-term performance in a wide range of dose-rates (e.g. 1–10 Gy/hr in LHC endcap calorimeters) and recovery periods from minutes to many months. In this respect, it is essential to develop reliable modeling to track detector calibration and long-term performance under adverse radiation conditions.

- It is cost prohibitive to produce a large number of doped and structured fibers with systematically varied parameters. Thus far, we have attempted to make logical choices for increasingly more performant fiber in terms of radiation-hardness. Although ray tracing tools exist (e.g. GEANT4), however, to the best of our knowledge, molecular level simulations to investigate radiation effects in doped fused-silica are not yet available.

Acknowledgments

This work has been supported by the US Department of Energy, Office of Science (DE-SC0015592), the Akdeniz University Scientific Research Projects Coordination Department (FDK-2017-2461), and the Scientific and Technological Research Council of Turkey, TÜBITAK, (No. 1059B141601412). We thank Professor A. Vedda and her group from Milan (Bicocca and INFN)

2019 JINST 14 P03020

for continued collaboration and illuminative discussions. We extend our thanks to Professor A. Belloni and his colleagues for making irradiations at the University of Maryland Cobalt-60 Panoramic Irradiator possible. We are grateful to Dr. M. Barnes from Texas Tech's Department of Geosciences for her meticulous work on mass spectroscopy. We acknowledge the continued support of Professors Nuri Unal, Ismail Boztosun, and Yusuf Sucu, who helped establish a scientific collaboration between the Akdeniz and Texas Tech Universities. Jim Clarkin and Teo Tichindelean from Polymicro Technologies are thanked for their expertise, continued interest, and commitment to this R&D project.

References

[1] N. Akchurin et al., *Effects of radiation and their consequences for the performance of the forward calorimeters in the CMS experiment*, *Nucl. Instrum. Meth.* **B 187** (2002) 66.

[2] I. Dumanoglu et al., *Radiation-hardness studies of high OH^- content quartz fibres irradiated with 500 MeV electrons*, *Nucl. Instrum. Meth.* **A 490** (2002) 444.

[3] N. Akchurin and R. Wigmans, *Quartz fibers as active elements in detectors for particle physics*, *Rev. Sci. Instrum.* **74** (2003) 2955.

[4] R.D. Thomas, *Study of radiation hardness of optical fibers*, Thesis, Texas Tech University, U.S.A. (2004).

[5] K. Cankoçak et al., *Radiation-hardness measurements of high OH^- content quartz fibres irradiated with* 24 *GeV protons up to* 1.25 *Grad*, *Nucl. Instrum. Meth.* **A 585** (2008) 20.

[6] M. Neff, V. Romano and W. Lüthy, *Metal-doped fibres for broadband emission: Fabrication with granulated oxides*, *Opt. Mater.* **31** (2008) 247.

[7] S. Braccini et al., *A beam monitor detector based on doped silica and optical fibres*, 2012 *JINST* **7** T02001.

[8] E. Anoikin et al., *UV and gamma radiation damage in silica glass and fibres doped with germanium and cerium*, *Nucl. Instrum. Meth.* **B 65** (1992) 392.

[9] E.R. Rand et al., *Luminescence studies of Cerium(III) incorporated in silica gels prepared using sol-gel methods*, *Inorg. Chim. Acta* **233** (1995) 71.

[10] G. Malashkevich, E. Poddenezhny, I. Melnichenko and A. Boiko, *Optical centers of cerium in silica glasses obtained by the sol-gel process*, *J. Non-Cryst. Sol.* **188** (1995) 107.

[11] G. Q. Xu, Z. X. Zheng, W. M. Tang and Y. C. Wu, *Spectroscopic properties of Ce^{3+} doped silica annealed at different temperatures*, *J. Lumin.* **124** (2007) 151.

[12] N. Chiodini et al., *High-efficiency SiO_2:Ce^{3+} glass scintillators*, *Applied Physics Letters* **81** (2002) 4374.

[13] A. Vedda et al., *Ce^{3+}-doped fibers for remote radiation dosimetry*, *Appl. Phys. Lett.* **85** (2004) 6356.

[14] M. Carrara et al., *Characterization of a Ce^{3+} doped SiO_2 optical dosimeter for dose measurements in hdr brachytherapy*, *Rad. Meas.* **56** (2013) 312.

[15] N. Caretto et al., *Feasibility of dose assessment in radiological diagnostic equipments using Ce-doped radio-luminescent optical fibers*, *Nucl. Instrum. Meth.* **A 612** (2010) 407.

[16] D. L. Griscom, M. E. Gingerich and E. J. Friebele, *Radiation-induced defects in glasses: origin of power-law dependence of concentration on dose*, *Phys. Rev. Lett.* **71** (1993) 1019.

2019 JINST 14 P03020

[17] V.A. Mashkov, W.R. Austin, L. Zhang and R.G. Leisure, *Fundamental Role of Creation and Activation in Radiation-Induced Defect Production in High-Purity Amorphous SiO_2*, Phys. Rev. Lett. **76** (1996) 2926.

[18] C.D. Marshall, J.A. Speth and S.A. Payne, *Induced optical absorption in gamma, neutron and ultraviolet irradiated fused quartz and silica*, J. Non-Cryst. Sol. **212** (1997) 59.

[19] N. Akchurin et al., *Cerium-doped scintillating fused-silica fibers*, 2018 *JINST* **13** P04010.

[20] P. Gorodetzky et al., *Quartz fiber calorimetry*, Nucl. Instrum. Meth. **A 361** (1995) 161.

[21] N. Akchurin et al., *Electron detection with a dual-readout calorimeter*, Nucl. Instrum. Meth. **A 536** (2005) 29.

[22] X. Sun et al., *Fluorescence properties and energy level structure of ce-doped silica fiber materials*, Opt. Mater. Expr. **7** (2017) 751.

[23] Y. Ishii et al., *Preparation of cerium-activated silica glasses: phosphorus and aluminum codoping effects on absorption and fluorescence properties*, J. Amer. Ceramic Soc. **70** (1987) 72.

[24] B.P. Fox et al., *Gamma radiation effects in Yb-doped optical fiber*, Proc. SPIE **6453** (2007) 6453.

[25] A.V. Faustov et al., *Comparison of gamma-radiation induced attenuation in Al-doped, P-doped and Ge-doped fibres for dosimetry*, IEEE Trans. Nucl. Sci. **60** (2013) 2511.

[26] Y. Kim et al., *Radiation-induced optical attenuation of Co/Fe Co-doped alumino-silicate optical fiber for radiation dosimeter application*, Proc. SPIE **8794** (2013) 8794.

[27] M. Paul et al., *Gamma ray radiation induced absorption in Ti doped single mode optical fibres at low dose levels*, Opt. Mater. **29** (2007) 738.

[28] D.L. Griscom, *Trapped-electron centers in pure and doped glassy silica: A review and synthesis*, J. Non.Cryst. Sol. **357** (2011) 1945.

[29] L.E. Halliburton, N. Koumvakalis, M.E. Markes and J.J. Martin, *Radiation effects in crystalline SiO_2: The role of aluminum*, J. Appl. Phys. **52** (1981) 3565.

[30] D.L. Griscom, M.E. Gingerich and E.J. Friebele, *Model for the dose, dose-rate and temperature dependence of radiation-induced loss in optical fibers*, IEEE Trans. Nucl. Sci. **41** (1994) 523.

[31] P. Borgermans and B. Brichard, *Kinetic models and spectral dependencies of the radiation-induced attenuation in pure silica fibers*, IEEE Trans. Nucl. Sci. **49** (2002) 1439.

[32] D.T.H. Liu and A.R. Johnston, *Theory of radiation-induced absorption in optical fibers*, Opt. Lett. **19** (1994) 548.

[33] R.A.B. Devine and J. Arndt, *Correlated defect creation and dose-dependent radiation sensitivity in amorphous SiO_2*, Phys. Rev. **B 39** (1989) 5132.

[34] D. L. Griscom, *Fractal kinetics of radiation-induced point-defect formation and decay in amorphous insulators: application to color centers in silica-based optical fibers*, Phys. Rev. **B 64** (2001) 174.

[35] E. Mies and L. Soto, *Characterization of the radiation sensitivity of single-mode optical fibers*, in the proceedings of the *International Conference on Integrated Optics Optical Fiber Communication (IOOC-ECOC85)*, October 1–4, Venice, Italy (1985).

[36] L. Giacomazzi et al., *Optical absorption spectra of P defects in vitreous silica*, Opt. Mater. Expr. **8** (2018) 385.

2019 JINST 14 P03020

[37] D.L. Griscom, E.J. Friebele, K.J. Long and J.W. Fleming, *Fundamental defect centers in glass: Electron spin resonance and optical absorption studies of irradiated phosphorus doped silica glass and optical fibers*, *J. Appl. Phys.* **54** (1983) 3743.

[38] M. Paul et al., *Radiation response behavior of high phosphorous doped step-index multimode optical fibers under low dose gamma irradiation*, *J. non-Cryst. Sol.* **355** (2009) 1496.

[39] S. Girard et al., *Radiation effects on silica-based optical fibers: Recent advances and future challenges*, *IEEE Trans. Nucl. Sci* **60** (2013) 2015.

[40] E.J. Friebele, C.G. Askins and M.E. Gingerich, *Effect of low dose rate irradiation on doped silica core optical fibers*, *Appl. Opt.* **23** (1984) 4202.

[41] T. Wijnands et al., *Optical absorption in commercial single mode optical fibers in a high energy physics radiation field*, *IEEE Trans. Nucl. Sci.* **55** (2008) 2216.

2019 JINST 14 P03020